Supplementary materials

Robust phase sensing via a nonlinear parity-time symmetric system

Dong-Yan Chen, Lei Dong*, and Qing-An Huang*

Key Laboratory of MEMS of the Ministry of Education, Southeast University, Nanjing 210096, China.

*e-mail: dl@seu.edu.cn; hqa@seu.edu.cn

Contents

S1. Basic equations of PT-symmetric *LC* sensors

The sensor under consideration consists of a pair of capacitively coupled parallel *RCL* resonators[1], as indicated in Fig. S1. The loss resonator is characterized by resistance R_2, capacitance C_2 and inductance L_2, with its node voltage denoted as $v_2(t)$. The gain resonator is characterized by resistance R_1, capacitance C_1 and inductance L_1, with its node voltage denoted as $v_1(t)$. The capacitance C_2 is utilized for sensing, meaning that it changes in response to the parameters of interest. The resistance R_1 is implemented using a THS4304 operational amplifier (OA) for negative resistance, suggesting that R_1 is dependent of the amplitude of node voltage $v_1(t)$. Specifically, $R_1 = -R_a R_c / R_b$ within the linear operation region of the OA. The coupling capacitance is denoted by C_C. For the purposes of this analysis, it is assumed that $C_1 = C_2 = C$ and $L_1 = L_2 = L$.

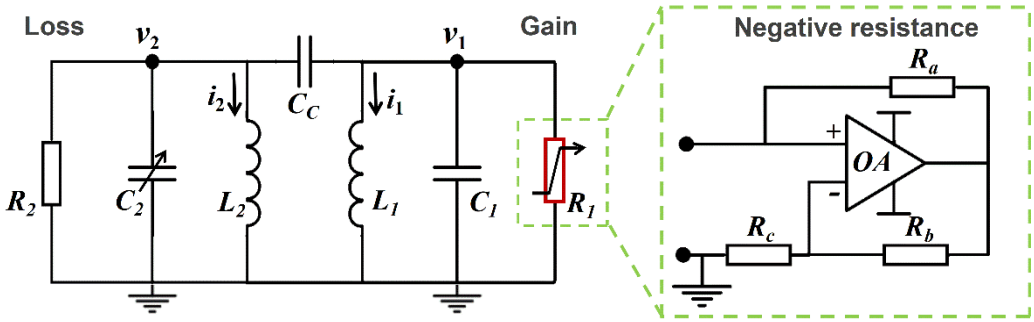

Supplementary Figure 1: Schematic of a pair of capacitively coupled parallel *RCL* resonators.

The relationship between voltage $v(t)$ and current $i(t)$ for resistance, capacitance, and inductance is given by, respectively,

$$\begin{aligned} i(t) &= \frac{v(t)}{R} \\ i(t) &= C\frac{dv(t)}{dt} \\ v(t) = L\frac{di(t)}{dt}, or\ \ i(t) &= \frac{1}{L}\int_0^t v(t)dt \end{aligned} \quad . \tag{S1}$$

Applying Kirchoff's current law for a pair of capacitively coupled parallel *RCL* resonators shown in Fig. S1 leads to

$$\begin{aligned} &\frac{1}{R_1}\frac{dv_1(t)}{dt} + C\frac{d^2v_1(t)}{dt^2} + \frac{1}{L}v_1(t) - C_C\left(\frac{d^2v_2(t)}{dt^2} - \frac{d^2v_1(t)}{dt^2}\right) = 0 \\ &\frac{1}{R_2}\frac{dv_2(t)}{dt} + C\frac{d^2v_2(t)}{dt^2} + \frac{1}{L}v_2(t) - C_C\left(\frac{d^2v_1(t)}{dt^2} - \frac{d^2v_2(t)}{dt^2}\right) = 0 \end{aligned} \quad . \tag{S2}$$

Taking time-harmonic solutions, one has

$$v_n(t) = V_n e^{i\omega t} = V_n e^{i\lambda\tau} \qquad (n = 1,2) \tag{S3}$$

where V_n $(n = 1,2)$ represents the complex amplitude of node voltages, $\lambda = \omega/\omega_0$ is the scaled angular frequency, $\tau = \omega_0 t$ is the rescaled time, and $\omega_0 = 1/\sqrt{LC}$ is the resonant frequency of an uncoupled *LC* resonator, respectively.

Inserting Eq. (S3) into Eq. (S2) yields

$$\begin{aligned} -i\lambda g V_1 - \lambda^2 V_1 + V_1 - \mu\lambda^2 V_1 + \mu\lambda^2 V_2 = 0 \\ +i\lambda\gamma V_2 - \lambda^2 V_2 + V_2 - \mu\lambda^2 V_2 + \mu\lambda^2 V_1 = 0 \end{aligned} \tag{S4}$$

with

$$g = -\frac{1}{R_1}\sqrt{\frac{L}{C}}$$
$$\gamma = \frac{1}{R_2}\sqrt{\frac{L}{C}} \qquad (S5)$$
$$\mu = \frac{C_C}{C}$$

where g, γ, and μ stand for the gain, loss, and coupling factor, respectively. In cases where the coupling is relatively weak, that is, $\mu \ll 1$, λ is around 1. Furthermore, μ, g and γ may be assumed to be of the same order of magnitude. By employing Taylor's series expansion at $\lambda = 1$ and neglecting high-order terms, the following approximation can be derived

$$\begin{gathered}\lambda^2 \approx 1 + 2(\lambda - 1) \\ \gamma\lambda \approx \gamma + \gamma(\lambda - 1) \approx \gamma \\ g\lambda \approx g + g(\lambda - 1) \approx g \\ \mu\lambda^2 \approx \mu + 2\mu(\lambda - 1) \approx \mu\end{gathered} \quad . \qquad (S6)$$

Utilizing the aforementioned approximations, Eq. (S4) is reformulated as

$$\begin{bmatrix} 1 - \lambda - \frac{\mu}{2} - i\frac{g}{2} & \frac{\mu}{2} \\ \frac{\mu}{2} & 1 - \lambda - \frac{\mu}{2} + i\frac{\gamma}{2} \end{bmatrix} \begin{bmatrix} V_1 \\ \\ V_2 \end{bmatrix} = 0. \qquad (S7)$$

Given time-harmonic voltages of Eq. (S3), Eq. (S7) is equivalent to the following coupled-mode equations

$$\begin{gathered} -i\frac{d}{dt}\begin{bmatrix} v_1 \\ v_2 \end{bmatrix} = H\begin{bmatrix} v_1 \\ v_2 \end{bmatrix} \\ H = \begin{bmatrix} 1 - \frac{\mu}{2} - i\frac{g}{2} & \frac{\mu}{2} \\ \frac{\mu}{2} & 1 - \frac{\mu}{2} + i\frac{\gamma}{2} \end{bmatrix} \end{gathered} \qquad (S8)$$

where H is interpreted as the Hamiltonian, while λ is considered to be the frequency eigenvalue.

S2. PT-symmetric *LC* sensors with linear loss and linear gain

(a) In the absence of perturbation

In the context of a linear PT-symmetric system, the gain remains constant. Consequently, the characteristic equation corresponding to Eq. (S8) turns out to be

$$\left(1 - \lambda - \frac{\mu}{2} - i\frac{g}{2}\right)\left(1 - \lambda - \frac{\mu}{2} + i\frac{\gamma}{2}\right) - \left(\frac{\mu}{2}\right)^2 = 0. \qquad (S9)$$

By solving the characteristic equation, the frequency eigenvalue is found to be

$$\lambda_{\mp} = 1 - \frac{\mu}{2} + i\frac{\gamma - g}{4} \mp \frac{1}{4}\sqrt{4(\mu^2 - g\gamma) - (\gamma - g)^2}. \qquad (S10)$$

When the gain and loss parameters are balanced, that is, $g = \gamma$, Eq. (S10) is simplified as

$$\lambda_{\mp} = 1 - \frac{\mu}{2} \mp \frac{1}{2}\sqrt{\mu^2 - \gamma^2}. \qquad (S11)$$

As displayed in Eq. (S11), two real frequency eigenvalues are obtained for $\mu > \gamma$ where it is referred to as the exact PT-symmetry regime, while the frequency eigenvalues in complex conjugate pairs come for $\mu < \gamma$ where it is referred to as the broken PT-symmetry regime. The exact and broken PT-symmetry regimes are separated by an exceptional point (EP), at $\mu = \gamma$, where the frequency eigenvalues and corresponding eigenvectors coalesce, i.e., $\lambda_- = \lambda_+$. The findings presented in this study are in good agreement with those procured through direct solutions to Eq. (S4)[1].

Incorporating Eqs. (S10) and (11) into Eq. (S3) facilitates an intuitive comprehension of a frequency eigenvalue. In the time-domain, the real part of the frequency eigenvalue corresponds to the oscillation frequency. The negative imaginary part of the frequency eigenvalue indicates an exponential growing mode while its positive imaginary part indicates an exponential decaying mode. The unsteady-state oscillations of the system can be ascribed to the imaginary part of the frequency eigenvalue. Additionally, in the frequency-domain, the peak frequency corresponds to the real part of the frequency eigenvalue, while its imaginary part is associated with the linewidth.

In this study, our primary focus is on steady-state oscillations that necessitate the frequency eigenvalues to be real. This condition implies that, for a linear PT-symmetric system, $g = \gamma$ and $\mu \geq \gamma$. Upon substituting Eq. (S11) into Eq. (S7), we derive

$$\left(\frac{V_2}{V_1}\right)_{\mp} = \frac{1 - \lambda_{\mp} - \frac{\mu}{2} - i\frac{\gamma}{2}}{-\left(\frac{\mu}{2}\right)} \qquad (S12)$$

$$\left|\frac{V_2}{V_1}\right|_{\mp} = 1$$

$$\phi_- = \pi - \tan^{-1}\frac{\gamma}{\sqrt{\mu^2 - \gamma^2}} \qquad (S13)$$

$$\phi_+ = \tan^{-1}\frac{\gamma}{\sqrt{\mu^2 - \gamma^2}}$$

where $\phi_{\mp}$ denotes the phase difference between the gain and loss resonator. Fig. S2 illustrates the parametric evolution of the real frequency eigenvalue and their corresponding phases as a function of the loss/coupling (γ/μ). The result for $|V_2/V_1| = 1$ shows that the voltage oscillations on the gain and loss sides are of equal magnitude for both λ_- and λ_+. When $\gamma = 0$, it follows from Eq. (S11) and Eq. (S13) that $\lambda_- = 1 - \mu$ with $\phi_- = \pi$ and $\lambda_+ = 1$ with $\phi_+ = 0$. This suggests that both resonators oscillate out of phase at λ_-, while they oscillate in phase at λ_+. Notably, $\gamma = 0$ signifies the restoration of the PT-symmetric system to a Hermitian system. When $\mu = \gamma$, that is, at an EP, we have $\lambda_- = \lambda_+ = \lambda_{EP} = 1 - \mu/2$ and $\phi_- = \phi_+ = \phi_{EP} = \pi/2$, respectively.

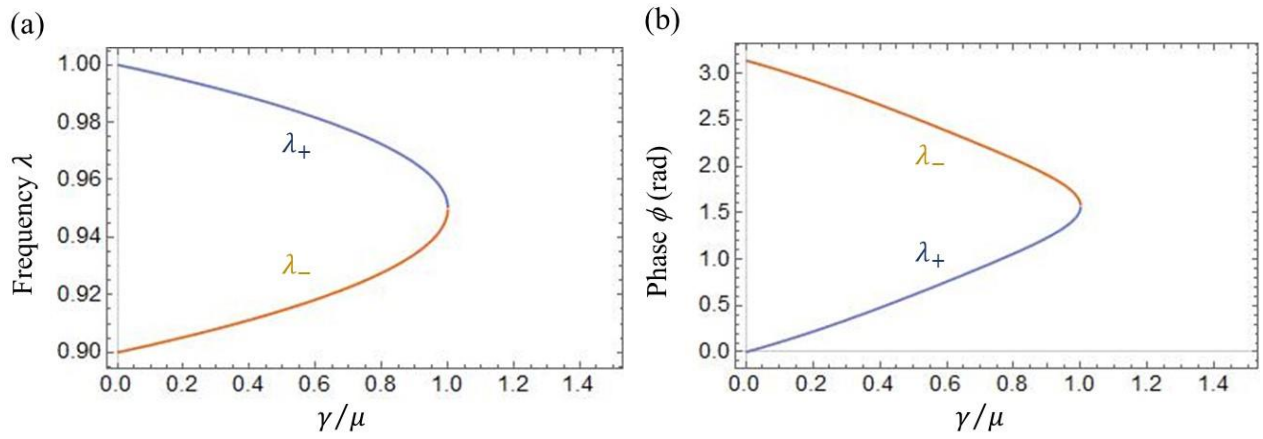

Supplementary Figure 2: (a) Parametric evolution of the real frequency eigenvalue as a function of the loss/coupling. (b) Parametric evolution of the phase as a function of the loss/coupling. The coupling parameter setting: $\mu = 0.1$.

(b) In the presence of perturbation

(i) A perturbation to the off-diagonal elements of the Hamiltonian

When a parameter to be sensed is applied to the coupling capacitance, the result is an alteration of the capacitance, notated as $C_c \to C_c + \Delta C_c = C_c(1+\delta_c)$, where $|\delta_c| = |\Delta C_c/\mathrm{C_c}| \ll 1$, and δ_c is referred to as a perturbation. Similar to the derivation of Eq. (S7), we have

$$\begin{bmatrix} 1-\lambda-\frac{\mu}{2}(1+\delta_c)-i\frac{g}{2} & \frac{\mu}{2}(1+\delta_c) \\ \frac{\mu}{2}(1+\delta_c) & 1-\lambda-\frac{\mu}{2}(1+\delta_c)+i\frac{\gamma}{2} \end{bmatrix}\begin{bmatrix} V_1 \\ V_2 \end{bmatrix} = 0. \quad (S14)$$

For the case where the gain and loss parameters are balanced ($g=\gamma$), the characteristic equation corresponding to Eq. (S14) turns out to be

$$\left(1-\lambda-\frac{\mu}{2}(1+\delta_c)-i\frac{\gamma}{2}\right)\left(1-\lambda-\frac{\mu}{2}(1+\delta_c)-\frac{\delta}{2}+i\frac{\gamma}{2}\right)-\left(\frac{\mu}{2}(1+\delta_c)\right)^2 = 0. \quad (S15)$$

By solving the characteristic equation, the frequency eigenvalue is found to be

$$\lambda_{\mp} = 1-\frac{\mu}{2}(1+\delta_c) \mp \frac{1}{2}\sqrt{[\mu(1+\delta_c)]^2-\gamma^2}. \quad (S16)$$

If the system is initially biased at an EP, i.e., $\gamma=\mu$, the frequency eigenvalue is then simplified to

$$\lambda_{\mp} = 1-\frac{\mu}{2}(1+\delta_c) \mp \frac{\mu}{2}\sqrt{(1+\delta_c)^2-1}. \quad (S17)$$

To ensure that the frequency eigenvalue is real, it is required that $\delta_c > 0$. The frequency eigenvalue splitting due to perturbation is given by

$$\Delta\lambda = \lambda_+ - \lambda_- = \mu\sqrt{(1+\delta_c)^2-1} \approx \sqrt{2}\mu\sqrt{\delta_c}. \quad (S18)$$

It shows that a perturbation drives a PT-symmetric system to move from an EP to PT-symmetric regimes. The frequency splitting approximately scales with the square-root of the perturbation with a scale factor of $\sqrt{2}\mu$. Given that $\delta_c \ll 1$, $\sqrt{\delta_c} \gg \delta_c$, suggesting an significant increase in sensitivity[2]. Meanwhile, however, a relatively small scale factor ($\mu \ll 1$) might offset, to some extent, the sensitivity enhanced owing to the square-root singularity. This sensitivity is represented as

$$\chi = \frac{\partial(\Delta\lambda)}{\partial\delta_c} = \frac{1}{\sqrt{2}}\mu\frac{1}{\sqrt{\delta_c}}\ . \quad (S19)$$

Inserting Eq. (S17) into Eq. (S14), it yields

$$\left(\frac{V_2}{V_1}\right)_{\mp} = \frac{1-\lambda_{\mp}-\frac{\mu}{2}(1+\delta_c)-i\frac{\mu}{2}}{-\left(\frac{\mu}{2}\right)(1+\delta_c)} \quad (S20)$$

$$\left|\frac{V_2}{V_1}\right|_{\mp} = 1$$

$$\phi_- = \pi - \tan^{-1}\frac{1}{\sqrt{(1+\delta_c)^2-1}} \approx \frac{\pi}{2}+\frac{\delta_c}{2} \quad (S21)$$

$$\phi_+ = \tan^{-1}\frac{1}{\sqrt{(1+\delta_c)^2-1}} \approx \frac{\pi}{2}-\frac{\delta_c}{2}\ .$$

The phase difference splitting linearly scales with the perturbation.

(ii) A perturbation to the diagonal elements of the Hamiltonian

When a parameter to be sensed induces a variation (ΔC) in the sensing capacitance of a loss resonator, this can be expressed as $C \to C + \Delta C = C(1+\delta)$, where $|\delta| = |\Delta C/C| \ll 1$. Similar to the derivation of Eq. (S7), we have

$$\begin{bmatrix} 1-\lambda-\frac{\mu}{2}-i\frac{g}{2} & \frac{\mu}{2} \\ \frac{\mu}{2} & 1-\lambda-\frac{\mu}{2}-\frac{\delta}{2}+i\frac{\gamma}{2} \end{bmatrix} \begin{bmatrix} V_1 \\ V_2 \end{bmatrix} = 0. \tag{S22}$$

For the case where the gain and loss parameters are balanced ($g = \gamma$), the characteristic equation corresponding to Eq. (S22) is found to be

$$\left(1-\lambda-\frac{\mu}{2}-i\frac{\gamma}{2}\right)\left(1-\lambda-\frac{\mu}{2}-\frac{\delta}{2}+i\frac{\gamma}{2}\right)-\left(\frac{\mu}{2}\right)^2 = 0. \tag{S23}$$

By solving the characteristic equation, the frequency eigenvalue turns out to be

$$\lambda_{\mp} = 1-\frac{\mu}{2}-\frac{\delta}{4} \mp \frac{1}{4}\sqrt{4(\mu^2-\gamma^2)+\delta^2-i4\gamma\delta}. \tag{S24}$$

If the system is initially biased at an EP, i.e., $\gamma = \mu$, the frequency eigenvalue is then simplified to

$$\lambda_{\mp} = 1-\frac{\mu}{2}-\frac{\delta}{4} \mp \frac{1}{4}\sqrt{\delta^2-i4\mu\delta}$$

$$= 1-\frac{\mu}{2}-\frac{\delta}{4} \mp \frac{1}{4\sqrt{2}}\left(\sqrt{\delta^2+\sqrt{(4\mu\delta)^2+\delta^4}}+i\sqrt{-\delta^2+\sqrt{(4\mu\delta)^2+\delta^4}}\right)$$

$$\approx 1-\frac{\mu}{2}-\frac{\delta}{4} \mp \frac{1}{2}\sqrt{\frac{\mu}{2}}\sqrt{\delta} \mp i\frac{1}{2}\sqrt{\frac{\mu}{2}}\sqrt{\delta} \tag{S25}$$

where a series expansion around $\delta = 0$ is employed. It is apparent from Eq. (S11) and Eq. (S25) that the PT-symmetric *LC* sensor, when initially biased at an EP, exhibits a steady-state oscillation at frequency $\lambda = 1-\mu/2$, but a perturbation causes a splitting of the frequency into the complex frequencies (λ_- and λ_+). As we discussed above, in the time-domain, the imaginary part of the frequency eigenvalue induces unsteady-state oscillations, while in the frequency-domain, the peak frequency corresponds to the real part of the frequency eigenvalue and its imaginary part is associated with the linewidth. According to Eq. (S25), the frequency splitting is given by

$$\Delta\lambda = \lambda_+ - \lambda_- \approx \sqrt{\frac{\mu}{2}}\sqrt{\delta}. \tag{S26}$$

Obviously, the frequency splitting due to a small perturbation follows the square-root singularity[3], which leads to an enhanced sensing compared with a linear response of Hermitian systems. Nevertheless, the complex frequency eigenvalue results in a spectrum broadening and sets the fundamental resolution limit.

S3. PT-symmetric *LC* sensors with linear loss and nonlinear saturable gain

For PT-symmetric *LC* sensors, as depicted in Fig. S1, negative resistance is achieved through an operational amplifier. This suggests that the negative resistance (R_1) depends upon the amplitude ($|V_1|$) of the node voltage $v_1(t)$. Consequently, $g(|V_1|) = -\sqrt{L/C}/R_1$ is also amplitude-dependent. It should be noted that at higher amplitudes, the gain inevitably saturates, and it is herein referred to as the saturation gain g_s. In linear PT-symmetric systems, we set a fixed gain and calculate the frequency eigenvalues, however, in PT-symmetric systems with nonlinear saturable gain, the gain becomes amplitude-dependent. An approach to solve the characteristic equation for frequency eigenvalues significantly differs from that of linear PT-symmetric systems[4]. In this work, since our interest is focused on steady-state oscillations, we require the frequency eigenvalues to be real. Hence, we look for a steady-state solution to the characteristic equation with a real λ while allowing g to be amplitude dependent. The gain supplying energy into the system varies with the oscillation amplitude. According to the minimum energy principle in physics, a system always needs to adjust itself to minimize its total energy and maintain a stable equilibrium state. Accordingly, for circumstances where there are multiple real solutions for the steady-state mode, the mode demanding the least gain will evolve to its steady state and saturate out the gain, thereby inhibiting other modes from accessing the requisite gain for steady-state oscillation. Correspondingly, under steady-state oscillations, there only exists the mode that possesses both the real frequency eigenvalue and the lowest saturation gain.

(a) In the absence of perturbation

For an instance where there is no perturbation to the sensing capacitance in a loss resonator, we take λ as a real, replace the gain g by the saturated gain g_s, and separate the real and imaginary parts of characteristic equation Eq. (S9), resulting in

$$\left(1-\lambda-\frac{\mu}{2}\right)^2+\frac{g_s\gamma}{4}-\left(\frac{\mu}{2}\right)^2+i\left(1-\lambda-\frac{\mu}{2}\right)\left(\frac{\gamma}{2}-\frac{g_s}{2}\right)=0. \tag{S27}$$

To ensure that the frequency eigenvalue is real, both the real and imaginary parts of Eq. (S27) must be simultaneously equal to zero. This constraint leads to

$$\left(1-\lambda-\frac{\mu}{2}\right)\left(\frac{\gamma}{2}-\frac{g_s}{2}\right)=0 \tag{S28}$$

$$\left(1-\lambda-\frac{\mu}{2}\right)^2+\frac{g_s\gamma}{4}-\left(\frac{\mu}{2}\right)^2=0. \tag{S29}$$

Two circumstances can meet the requirements of Eq. (S28). When the two circumstances are incorporated into Eq. (S29), it yields, respectively,

$$\begin{cases} g_s=\gamma \\ \lambda_{\mp}=1-\dfrac{\mu}{2}\mp\dfrac{1}{2}\sqrt{\mu^2-\gamma^2} \end{cases} \tag{S30}$$

and

$$\begin{cases} \lambda_b=1-\dfrac{\mu}{2} \\ g_s=\dfrac{\mu^2}{\gamma} \end{cases}. \tag{S31}$$

From Eqs. (S30) and (S31), it is apparent that for $\mu>\gamma$, $\lambda_{\mp}$ and λ_b are all real, but the mode λ_b requires the higher saturation gain (μ^2/γ) than the modes $\lambda_{\mp}$ that require the saturation gain (γ). As a result, physically,

the mode λ_b does not occur under steady-state oscillation for $\mu > \gamma$. For $\mu < \gamma$, however, only λ_b is real, while for $\mu = \gamma$, we have $\lambda_{\mp} = 1 - \mu/2$. Similar to the derivation of Eqs. (S12) and (S13), it produces

$$\begin{cases} \lambda_{\mp} = 1 - \dfrac{\mu}{2} \mp \dfrac{1}{2}\sqrt{\mu^2 - \gamma^2} \\ \left|\dfrac{V_2}{V_1}\right|_{\mp} = 1 \\ \phi_- = \pi - \tan^{-1}\dfrac{\gamma}{\sqrt{\mu^2 - \gamma^2}} \\ \phi_+ = \tan^{-1}\dfrac{\gamma}{\sqrt{\mu^2 - \gamma^2}} \end{cases} \qquad (\mu \geq \gamma, g_s = \gamma) \qquad (S32)$$

$$\begin{cases} \lambda_b = 1 - \dfrac{\mu}{2} \\ \left|\dfrac{V_2}{V_1}\right|_b = \dfrac{\mu}{\gamma} \\ \phi_b = \dfrac{\pi}{2} \end{cases} \qquad \left(\mu < \gamma, g_s = \frac{\mu^2}{\gamma}\right). \qquad (S33)$$

Fig. S3 illustrates the parametric evolution of the real frequency eigenvalue and their corresponding phases as a function of the loss/coupling (γ/μ). Fig. S4 provides the amplitude ratio and their corresponding saturation gain as a function of the loss/coupling (γ/μ). When $\mu = \gamma$, we have $\lambda_- = \lambda_+ = \lambda_{EP} = 1 - \mu/2$ and $\phi_- = \phi_+ = \phi_{EP} = \pi/2$, respectively.

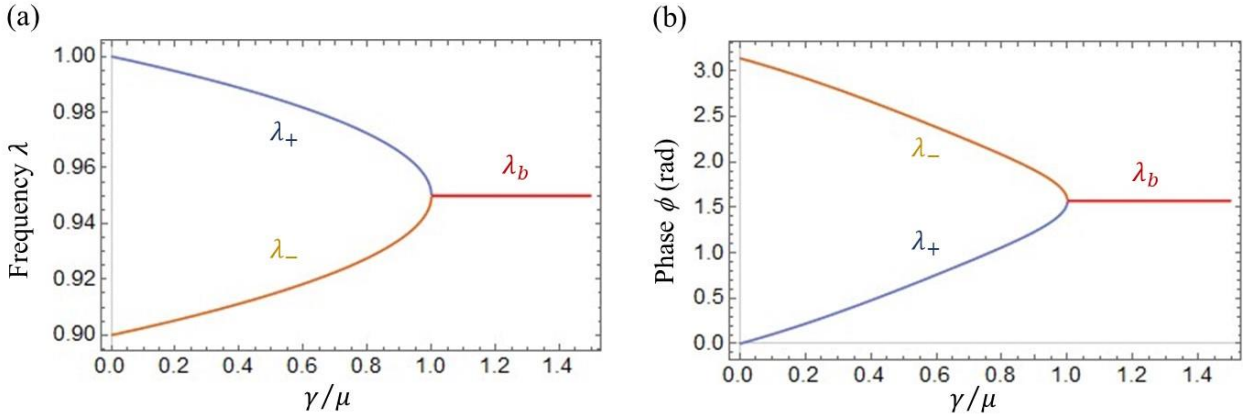

Supplementary Figure 3: (a) Parametric evolution of the real frequency eigenvalue as a function of the loss/coupling. (b) Parametric evolution of the phase as a function of the loss/coupling. The coupling parameter setting: $\mu = 0.1$.

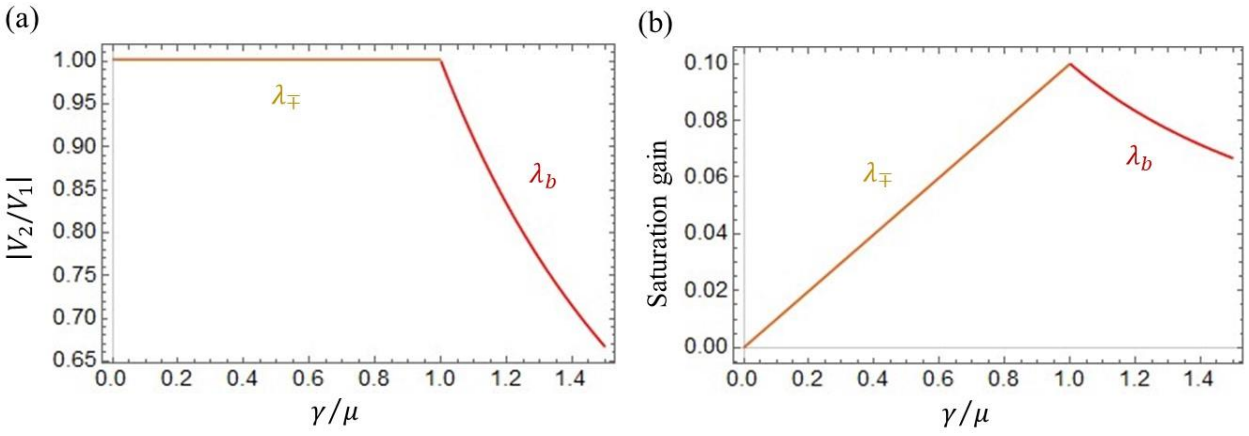

Supplementary Figure 4: (a) The amplitude ratio as a function of the loss/coupling. (b) The saturation gain as a function of the loss/coupling. The coupling parameter setting: $\mu = 0.1$.

For $\mu \geq \gamma$, the results presented by Eq. (S32) for a nonlinear PT-symmetric system are the same as those given by Eqs. (S11), (S12) and (S13) for a linear PT-symmetric system. However, it is imperative to note that the underlying physical mechanisms differ significantly between them. In the context of the linear PT system, PT-symmetry is scrupulously maintained by selecting a system Hamiltonian that inherently possesses PT-symmetry, achieved by setting $g = \gamma$, while for the nonlinear PT system, PT-symmetry spontaneously arises from the gain saturation mechanism, ensuring that the system automatically exhibits PT-symmetry at steady state. In particular, for $\mu < \gamma$, the linear PT system does not exhibit steady-state oscillation, whereas the nonlinear PT system, as a consequence of its gain saturation mechanism, oscillates at a steady state with a frequency of $1 - \mu/2$. As illustrated in Figs. S4 and S5, when $\mu < \gamma$, the saturation gain necessary for the system decreases as the coupling diminishes. This is because the amplitude of the loss resonator, which correlates to the required energy, is reduced. The results illustrated in this study align well with those obtained for a nonlinear PT-symmetric *LC* system involving inductive coupling[4].

(b) In the presence of perturbation

(i) A perturbation to the off-diagonal elements of the Hamiltonian

When a parameter to be sensed is applied to the coupling capacitance, the result is an alteration of the capacitance, notated as $C_c \to C_c + \Delta C_c = C_c(1 + \delta_c)$, where $|\delta_c| = |\Delta C_c / \mathrm{C_c}| \ll 1$. We can substitute the gain g in Eq. (S14) with the saturated gain g_s. By separating the real and imaginary parts of characteristic equation for Eq. (S15) with g replaced by g_s, we then obtain

$$\left(1 - \lambda - \frac{\mu}{2}(1 + \delta_c)\right)^2 + \frac{g_s \gamma}{4} - \left(\frac{\mu}{2}(1 + \delta_c)\right)^2 + i\left(1 - \lambda - \frac{\mu}{2}(1 + \delta_c)\right)\left(\frac{\gamma}{2} - \frac{g_s}{2}\right) = 0. \qquad (S34)$$

To ensure that the frequency eigenvalue is real, both the real and imaginary parts of Eq. (S34) must be simultaneously equal to zero. This constraint leads to

$$\left(1 - \lambda - \frac{\mu}{2}(1 + \delta_c)\right)\left(\frac{\gamma}{2} - \frac{g_s}{2}\right) = 0 \qquad (S35)$$

$$\left(1 - \lambda - \frac{\mu}{2}(1 + \delta_c)\right)^2 + \frac{g_s \gamma}{4} - \left(\frac{\mu}{2}(1 + \delta_c)\right)^2 = 0. \qquad (S36)$$

Two circumstances can meet the requirements of Eq. (S35). When the two circumstances are incorporated into Eq. (S36), it yields, respectively,

$$\begin{cases} g_s = \gamma \\ \lambda_{\mp} = 1 - \dfrac{\mu}{2}(1 + \delta_c) \mp \dfrac{1}{2}\sqrt{[\mu(1 + \delta_c)]^2 - \gamma^2} \end{cases} \qquad (S37)$$

and

$$\begin{cases} \lambda_b = 1 - \dfrac{\mu}{2}(1 + \delta_c) \\ g_s = \dfrac{[\mu(1 + \delta_c)]^2}{\gamma} \end{cases} . \qquad (S38)$$

Under steady-state oscillations, there only exist the mode that possesses both the real frequency eigenvalue and the lowest saturation gain. Similar to the derivation of Eqs. (S12) and (S13), it produces

$$\begin{cases} \lambda_{\mp} = 1 - \dfrac{\mu}{2}(1+\delta_c) \mp \dfrac{1}{2}\sqrt{[\mu(1+\delta_c)]^2 - \gamma^2} \\ \left|\dfrac{V_2}{V_1}\right|_{\mp} = 1 \\ \phi_- = \pi - \tan^{-1}\dfrac{\gamma}{\sqrt{[\mu(1+\delta_c)]^2 - \gamma^2}} \\ \phi_+ = \tan^{-1}\dfrac{\gamma}{\sqrt{[\mu(1+\delta_c)]^2 - \gamma^2}} \end{cases} \qquad (\mu(1+\delta_c) \geq \gamma, g_s = \gamma) \qquad (S39)$$

$$\begin{cases} \lambda_b = 1 - \dfrac{\mu}{2}(1+\delta_c) \\ \left|\dfrac{V_2}{V_1}\right|_b = \dfrac{\mu}{\gamma}(1+\delta_c) \\ \phi_b = \dfrac{\pi}{2} \end{cases} \qquad \left(\mu(1+\delta_c) < \gamma, g_s = \frac{[\mu(1+\delta_c)]^2}{\gamma}\right). \qquad (S40)$$

When the system is initially at an EP ($\mu = \gamma$), the frequency eigenvalue for Eq. (S39) is then simplified to

$$\lambda_{\mp} = 1 - \frac{\mu}{2}(1+\delta_c) \mp \frac{\mu}{2}\sqrt{(1+\delta_c)^2 - 1}. \qquad (S41)$$

where $\delta_c > 0$. The frequency eigenvalue splitting due to perturbation is written as

$$\Delta\lambda = \lambda_+ - \lambda_- = \mu\sqrt{(1+\delta_c)^2 - 1} \approx \sqrt{2}\mu\sqrt{\delta_c}. \qquad (S42)$$

The results presented by Eqs. (S39), (S41) and (S42) for a nonlinear PT-symmetric system are the same as those given by Eqs. (S16)~(S21) for a linear PT-symmetric system. However, as discussed above, the underlying physical mechanisms differ significantly between them. In particular, for $\mu(1+\delta_c) < \gamma$, the linear PT system does not exhibit steady-state oscillation, whereas the nonlinear PT system, as a consequence of its gain saturation mechanism, oscillates at a steady state with a single frequency of $1 - \mu(1+\delta_c)/2$, that is, the frequency eigenvalue linearly scales with a perturbation. The results of Eqs. (S39)~(S42) are generally in good agreement with those obtained experimentally (Fig. 3 in Ref. [5]).

(ii) A perturbation to the diagonal elements of the Hamiltonian

When an external perturbation is applied to the sensing capacitance of a loss resonator, we can substitute the gain g in Eq. (S22) with the saturated gain g_s. This yields an equation that the voltage amplitude follows, given by

$$\begin{bmatrix} 1 - \lambda - \dfrac{\mu}{2} - i\dfrac{g_s}{2} & \dfrac{\mu}{2} \\ \dfrac{\mu}{2} & 1 - \lambda - \dfrac{\mu}{2} - \dfrac{\delta}{2} + i\dfrac{\gamma}{2} \end{bmatrix} \begin{bmatrix} V_1 \\ V_2 \end{bmatrix} = 0. \qquad (S43)$$

By separating the real and imaginary parts of characteristic equation for Eq. (S43), we obtain

$$\left(1 - \lambda - \frac{\mu}{2}\right)\left(1 - \lambda - \frac{\mu}{2} - \frac{\delta}{2}\right) + \frac{g_s\gamma}{4} - \left(\frac{\mu}{2}\right)^2 + i\left[\frac{\gamma}{2}\left(1 - \lambda - \frac{\mu}{2}\right) - \frac{g_s}{2}\left(1 - \lambda - \frac{\mu}{2} - \frac{\delta}{2}\right)\right] = 0. \qquad (S44)$$

To ensure that the frequency eigenvalue is real, both the real and imaginary parts of Eq. (S44) must be simultaneously equal to zero. This constraint leads to

$$\frac{\gamma}{2}\left(1-\lambda-\frac{\mu}{2}\right)-\frac{g_s}{2}\left(1-\lambda-\frac{\mu}{2}-\frac{\delta}{2}\right)=0 \tag{S45}$$

$$\left(1-\lambda-\frac{\mu}{2}\right)\left(1-\lambda-\frac{\mu}{2}-\frac{\delta}{2}\right)+\frac{g_s\gamma}{4}-\left(\frac{\mu}{2}\right)^2=0. \tag{S46}$$

Solving Eq. (S45) leads to

$$g_s=\gamma\frac{1-\lambda-\frac{\mu}{2}}{1-\lambda-\frac{\mu}{2}-\frac{\delta}{2}}\ . \tag{S47}$$

By inserting Eq. (S47) into Eq. (S46), we obtain

$$\left(1-\lambda-\frac{\mu}{2}\right)^3-\delta\left(1-\lambda-\frac{\mu}{2}\right)^2+\left[\left(\frac{\delta}{2}\right)^2+\left(\frac{\gamma}{2}\right)^2-\left(\frac{\mu}{2}\right)^2\right]\left(1-\lambda-\frac{\mu}{2}\right)+\left(\frac{\delta}{2}\right)\left(\frac{\mu}{2}\right)^2=0. \tag{S48}$$

Eq. (S48) is the cubic equation about a frequency eigenvalue λ. The roots of the cubic equation can be analytically given according to Cardano's formulas[6]. Cardano's notations are utilized here, represented by

$$\begin{cases} a=-\delta \\ b=\left(\frac{\delta}{2}\right)^2+\left(\frac{\gamma}{2}\right)^2-\left(\frac{\mu}{2}\right)^2 \\ c=\left(\frac{\delta}{2}\right)\left(\frac{\mu}{2}\right)^2 \\ q=\frac{1}{3}a^2-b \\ r=-\frac{2}{27}a^3+\frac{1}{3}ab-c \end{cases}. \tag{S49}$$

The frequency eigenvalue is found to be

$$\begin{cases} \lambda_1=1-\frac{\mu}{2}-\frac{\delta}{3}-\frac{2^{1/3}q}{\left(27r+3\sqrt{3}\sqrt{27r^2-4q^3}\right)^{1/3}}-\frac{\left(27r+3\sqrt{3}\sqrt{27r^2-4q^3}\right)^{1/3}}{3\times 2^{1/3}} \\ \lambda_2=1-\frac{\mu}{2}-\frac{\delta}{3}+\frac{\left(1+i\sqrt{3}\right)q}{2^{2/3}\left(27r+3\sqrt{3}\sqrt{27r^2-4q^3}\right)^{1/3}}+\frac{\left(1-i\sqrt{3}\right)\left(27r+3\sqrt{3}\sqrt{27r^2-4q^3}\right)^{1/3}}{6\times 2^{1/3}} \\ \lambda_3=1-\frac{\mu}{2}-\frac{\delta}{3}+\frac{\left(1-i\sqrt{3}\right)q}{2^{2/3}\left(27r+3\sqrt{3}\sqrt{27r^2-4q^3}\right)^{1/3}}+\frac{\left(1+i\sqrt{3}\right)\left(27r+3\sqrt{3}\sqrt{27r^2-4q^3}\right)^{1/3}}{6\times 2^{1/3}} \end{cases}. \tag{S50}$$

According to Cardano's formulas, there are three real roots $(\lambda_1,\lambda_2,\lambda_3)$ if $4q^3\geq 27r^2$, while there is only one real root $(\lambda_1 or \lambda_2)$ if $4q^3<27r^2$. Depending on parameter settings (μ,γ and δ), there is either one, two, or three real roots.

For $\mu>\gamma$, Fig. S5 illustrates the real frequency eigenvalue and its corresponding saturation gain as a function of perturbation. It is evident that three real-valued roots only exist within the confines of very minor perturbations ($|\delta|\ll 1$). Nevertheless, as mentioned above, under steady-state oscillations, there only exist the mode that possesses both the real frequency eigenvalue and the lowest saturation gain. With reference to Fig. (S5b), it is clear that there is only λ_1 for $\delta<0$, while there is only λ_2 for $\delta>0$.

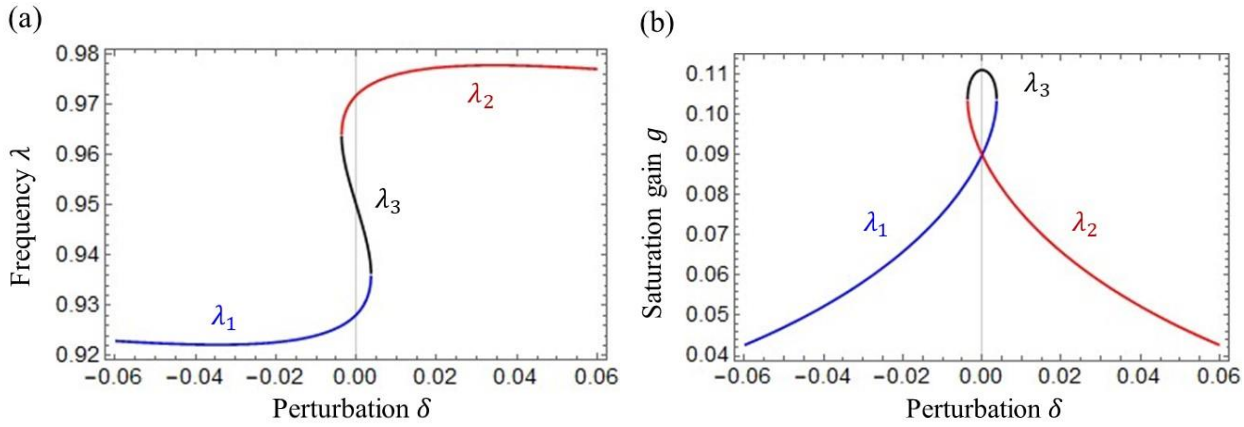

Supplementary Figure 5: (a) The real frequency eigenvalue as a function of perturbation. (b) The saturation gain, which corresponds to the real frequency eigenvalue, as a function of perturbation. The parameter setting: $\mu = 0.1$ and $\gamma = 0.09$.

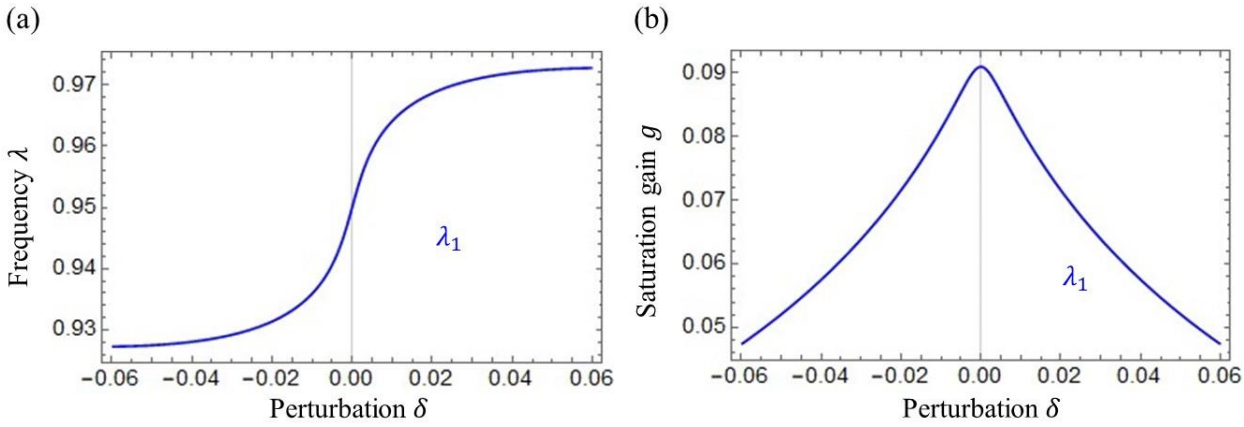

Supplementary Figure 6: (a) The real frequency eigenvalue as a function of perturbation. (b) The saturation gain, which corresponds to the real frequency eigenvalue, as a function of perturbation. The parameter setting: $\mu = 0.1$ and $\gamma = 0.11$.

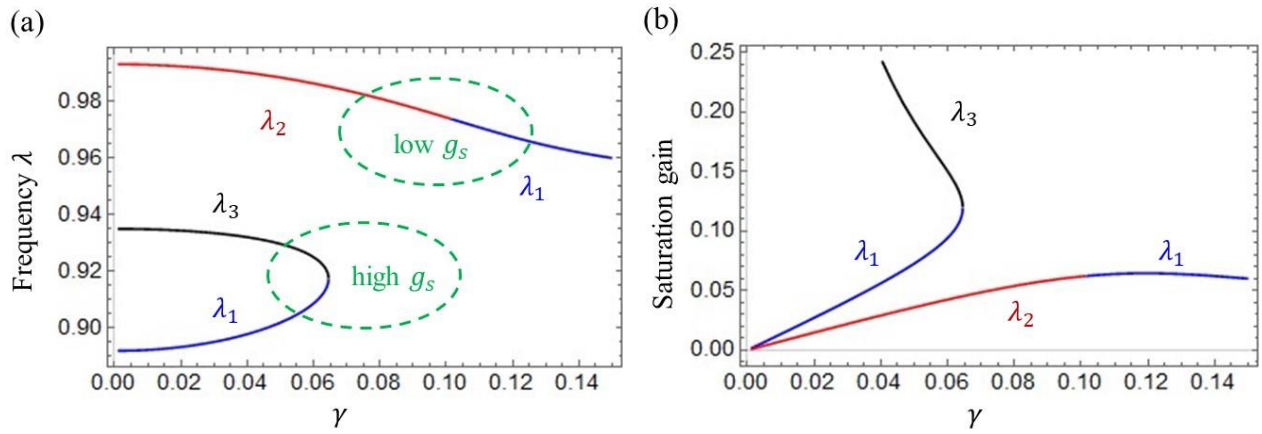

Supplementary Figure 7: (a) The real frequency eigenvalue as a function of loss. (b) The saturation gain, which corresponds to the real frequency eigenvalue, as a function of loss. The parameter setting: $\mu = 0.1$ and $\delta = 0.03$.

For $\mu < \gamma$, Fig. S6 illustrates the real frequency eigenvalue and its corresponding saturation gain as a function of perturbation. It is clear that there is only λ_1 for $\mp\delta$.

Fig. S7 depicts the real frequency eigenvalue and its corresponding saturation gain as a function of loss in the presence of perturbation. It is evident that there are three real roots in the low loss ($\gamma < \mu$), whereas there is only one real root in the high loss ($\gamma > \mu$). Nevertheless, as mentioned above, under steady-state oscillations, there only exist the mode that possesses both a real frequency eigenvalue and the lowest saturation gain. Accordingly, only λ_2 is present for $\gamma < \mu$, while only λ_1 is present for $\gamma > \mu$.

Our analysis indicates that, in the presence of perturbation, Eq. (S32) may have multiple real roots depending on the parameter settings (μ, γ and δ). However, under steady-state oscillations, only the mode with both a real frequency eigenvalue and the lowest saturation gain exists. As a result, regardless of the parameter settings, λ_3 is absent.

For $\mu = \gamma$, where the system is initially biased at an EP, Fig. S8 illustrates the real frequency eigenvalue and its corresponding saturation gain as a function of perturbation. It is clear that λ_2 is only present for $\delta > 0$ and λ_1 is only present for $\delta < 0$.

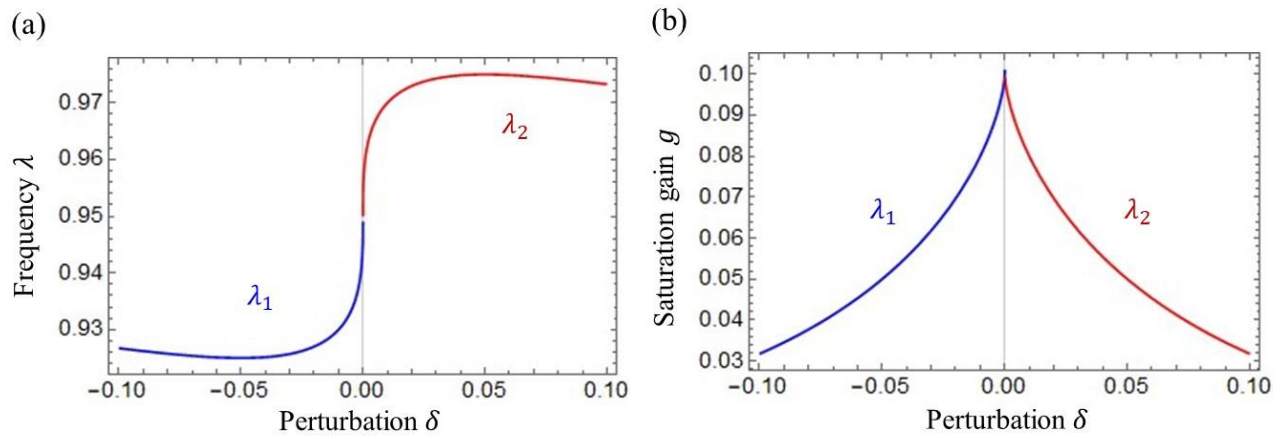

Supplementary Figure 8: (a) The real frequency eigenvalue as a function of perturbation. (b) The saturation gain, which corresponds to the real frequency eigenvalue, as a function of perturbation. The parameter setting: $\mu = 0.1$ and $\gamma = 0.1$.

In the case of our nonlinear EP sensor, we apply positive perturbations. To comprehend the behavior of a frequency eigenvalue intuitively, we employ the Taylor series expansion of λ_2 around $\delta = 0$ by utilizing constraint conditions where $\gamma = \mu$ and $\delta > 0$. The frequency eigenvalue is given by, to a first-order approximation

$$\lambda_2 \approx 1 - \frac{\mu}{2} - \frac{\delta}{3} + \frac{1}{2}\mu^{2/3}\delta^{1/3} \quad . \tag{S51}$$

Upon substituting Eq. (S51) into Eq. (S47), the resulting saturation gain is found to be

$$g_s = \gamma \frac{1 - \lambda_2 - \frac{\mu}{2}}{1 - \lambda_2 - \frac{\mu}{2} - \frac{\delta}{2}} \approx \gamma \left(\frac{\mu^{2/3}\delta^{1/3} - \frac{2\delta}{3}}{\mu^{2/3}\delta^{1/3} + \frac{\delta}{3}} \right) \quad . \tag{S52}$$

By substituting Eqs. (S51) and (S52) into Eq. (S43), we derive the following equation:

$$\frac{V_2}{V_1} = \frac{-\left(\frac{\mu}{2}\right)}{1 - \lambda_2 - \frac{\mu}{2} - \frac{\delta}{2} + i\frac{\gamma}{2}} \approx \frac{\mu}{\mu^{2/3}\delta^{1/3} + \frac{\delta}{3} - i\gamma} \tag{S53}$$

$$\left|\frac{V_2}{V_1}\right|^2 = \frac{\left(\frac{\mu}{2}\right)^2}{\left(1-\lambda_2-\frac{\mu}{2}-\frac{\delta}{2}\right)^2+\left(\frac{\gamma}{2}\right)^2} \approx \frac{\mu^2}{\left(\mu^{2/3}\delta^{1/3}+\frac{\delta}{3}\right)^2+\gamma^2} \tag{S54}$$

$$\phi = -\tan^{-1}\frac{\frac{\gamma}{2}}{1-\lambda_2-\frac{\mu}{2}-\frac{\delta}{2}} \approx \tan^{-1}\frac{\mu}{\mu^{2/3}\delta^{1/3}+\frac{\delta}{3}} \approx \frac{\pi}{2}-\left(\frac{\delta}{\mu}\right)^{1/3} \tag{S55}$$

where the Taylor series expansion is utilized for Eq. (S55) under conditions that $\gamma = \mu$ and $\delta > 0$.

Fig. S9 depicts the comparison between approximate and exact results for the real frequency eigenvalue, its associated saturation gain, amplitude ratio, and phase difference, as a function of perturbation. In each of these results, there is a good agreement between the approximate and exact solutions over a wide range of perturbations.

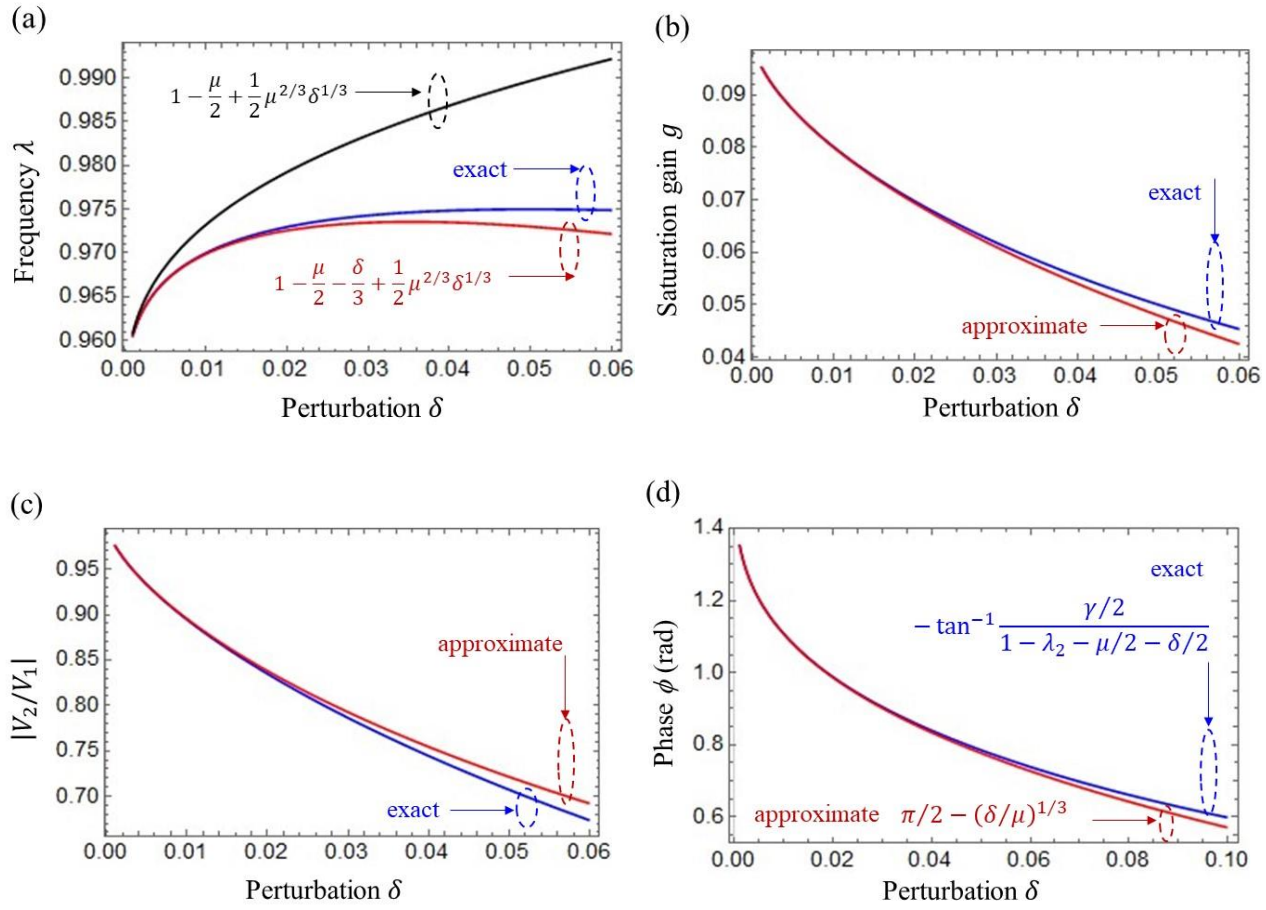

Supplementary Figure 9: Comparison of exact and approximate results. (a) The real frequency eigenvalue as a function of perturbation. For comparisons, the frequency eigenvalue ignoring $-\delta/3$ is also plotted. (b) The saturation gain as a function of perturbation. (c) Amplitude ratio as a function of perturbation. (d) The phase difference as a function of perturbation. The parameter setting: $\mu = 0.1$ and $\gamma = 0.1$.

From Eq. (S51), one can observe that the dependency of the frequency eigenvalue on the perturbation consists of two terms: a positive cubic-root responsivity and a negative linear responsivity, which are in opposition to each other. By using Eq. (51), solving $\partial\lambda_2/\partial\delta = 0$ approximately yields $\delta_T = \mu/2\sqrt{2} \approx 0.354\mu$, where δ_T is referred to as the turning point. When $\delta > \delta_T$, the frequency eigenvalue reduces as the perturbation increases, whereas when $\delta < \delta_T$, it increases with the perturbation.

If a system is initially biased at an EP, i.e., $\lambda = \lambda_{EP} = 1 - \mu/2$, a shift in the frequency eigenvalue owing to a perturbation is given by

$$\Delta\lambda = \lambda_2 - \lambda_{EP} \approx \frac{1}{2}\mu^{2/3}\delta^{1/3} - \frac{\delta}{3} \ . \tag{S56}$$

The sensitivity of the frequency eigenvalue to a perturbation is represented by

$$\chi_\lambda = \frac{\partial|\Delta\lambda|}{\partial\delta} \approx \frac{1}{6}\mu^{2/3}\delta^{-2/3} - \frac{1}{3}. \tag{S57}$$

From Eqs. (S56) and (S57), it is clear that in the limit of small perturbations, i.e., $\delta \ll \delta_T$, the frequency shift approximates a cube-root singularity of the perturbation, where the scale factor is $\mu^{2/3}/6$. Given that $\delta^{1/3} \gg \delta$ when $\delta \ll 1$, this leads to an enhanced sensing compared to the linear response of Hermitian systems. Nevertheless, the cube-root singularity remains valid only in the limit of small perturbations ($\delta \ll \delta_T$). The condition where $\delta \ll \delta_T$ needs to be satisfied if the cube-root singularity is dominant. This suggests that the dynamic range, defined as the ratio between the maximum and minimum perturbations that a sensor can detect, is considerably reduced.

It is clear from Eq. (S55) and Fig. (S9d) that the phase difference also exhibits a cube-root singularity across a wide range of perturbations. When the system is initially biased at an EP, i.e., $\phi_{EP} = \pi/2$, the shift in the phase difference owing to a perturbation is expressed as

$$\Delta\phi = \phi - \phi_{EP} \approx -\left(\frac{\delta}{\mu}\right)^{1/3}. \tag{S58}$$

The sensitivity of the phase difference to a perturbation is written as

$$\chi_\phi = \frac{\partial|\Delta\phi|}{\partial\delta} \approx \frac{1}{3}\mu^{-1/3}\delta^{-2/3}. \tag{S59}$$

Besides the broad dynamic range, the sensitivity scale factor for phase sensing is given by $\mu^{-1/3}/3$, which is equivalent to $2/\mu$ times the sensitivity scale for frequency sensing. Given that $\mu \ll 1$, this indicates that the sensitivity for phase sensing has increased by several orders of magnitude relative to frequency sensing. It should be noted that the sensitivity of a sensor is estimated as the product of its scale factor and its responsivity to perturbations.

Fig. S10 depicts the frequency eigenvalue and phase difference as a function of perturbation.

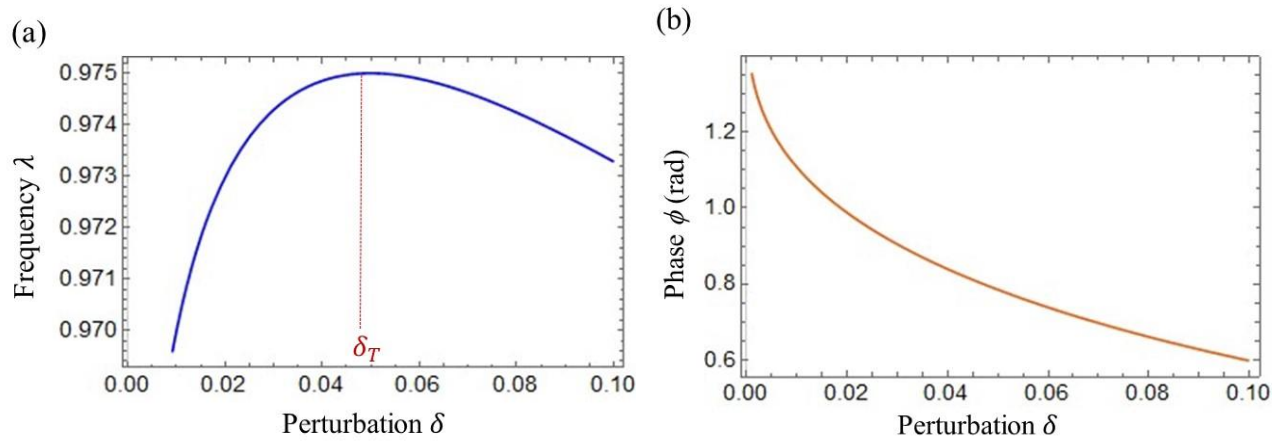

Supplementary Figure 10: The frequency eigenvalue and phase difference as a function of perturbation. (a) The frequency eigenvalue. (b) The phase difference. The parameter setting: $\mu = 0.1$ and $\gamma = 0.1$.

Fig. S11 illustrates the comparison of the sensitivity between the frequency eigenvalue and phase difference as a function of perturbation.

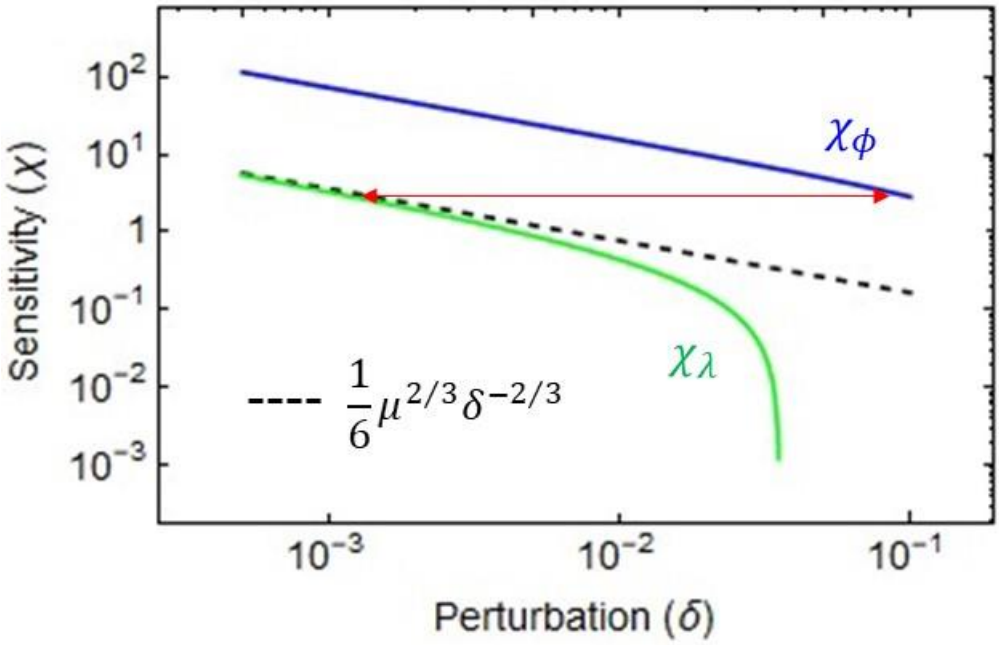

Supplementary Figure 11: Comparison of the sensitivity between the frequency eigenvalue and phase difference as a function of perturbation. The frequency eigenvalue corresponding to the cube-root singularity of perturbation is also provided. The arrow depicted in red signifies the enhancement in dynamic range. The parameter setting: $\mu = 0.1$ and $\gamma = 0.1$.

S4. ADS Simulation

Fig. S12 presents the schematic diagram of our nonlinear PT-symmetric LC system simulated using Advanced Design System (ADS). The core component, which provides negative resistance, is constructed using a nonlinear operational amplifier (THS4304 by Texas Instruments)[7]. In our simulations, we set $L_1 = L_2 = 1$ μH, $C_1 = C_2 = 249$ pF, and $R_2 = 800$ Ω, with the loss coefficient $\gamma \approx 0.08 \ll 1$. The coupling capacitance C_c is established at 22.5 pF ($\mu \approx 0.09$), allowing the system to function at the PT-symmetric regime close to an EP. However, it should be noted that proximity to the EP will destabilize the system, necessitating careful selection of the coupling coefficient. Capacitors C_3, C_4, C_5 and C_6 are employed to prevent interference from DC signals. Resistors R_4, R_5 and R_6 serve to clamp half of the DC supply voltage to the in-phase input of the operational amplifier. In both simulations and experiments, we ensure that the absolute value of the negative resistance R_1 is slightly less than the positive resistance R_2, enabling the system to initiate self-oscillation in the PT-symmetric LC system.

(a) Simulation setup

Fig. S12 illustrates the construction of a PT-symmetric circuit with an applied perturbation. By adjusting the transient time appropriately, we are able to observe the time domain oscillation waveform. The voltage phase between the gain and loss sides is obtained via simulation. The steady-state oscillation frequency can be determined by performing a Fourier transform (using the built-in simulator) on the stabilized time-domain signal over an arbitrarily long period of time.

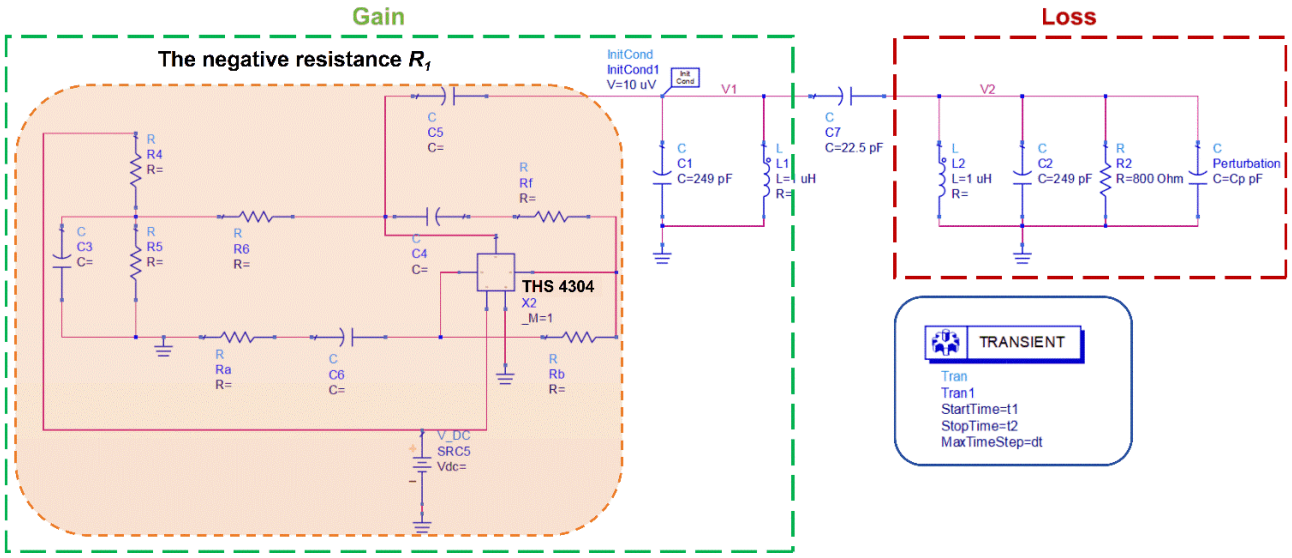

Supplementary Figure 12: Schematic diagram of the nonlinear PT symmetric system constructed by ADS.

(b) Time-domain and frequency-domain simulations

Fig. S13a depicts the time-domain node voltage of the gain and loss resonators, clearly demonstrating that the steady-state voltage on the loss side (v_2) precedes that on the gain side (v_1). A frequency spectrum analysis via fast Fourier transform (FFT), shown in Fig. S13b, corroborates that both the gain and loss resonators sustain steady-state oscillation at the same frequency. Furthermore, Fig. S13b reveals that perturbations do not induce a broadening of the frequency spectrum in the nonlinear PT symmetric system, thereby averting noise-induced degradation of sensor performance. The leading time Δt can be transformed into a phase difference through dividing it by the oscillation cycle T. The absolute value of the phase difference decreases with increasing the perturbation, affirming the consistency between the simulation and the theoretical prediction given by Eq. (S55).

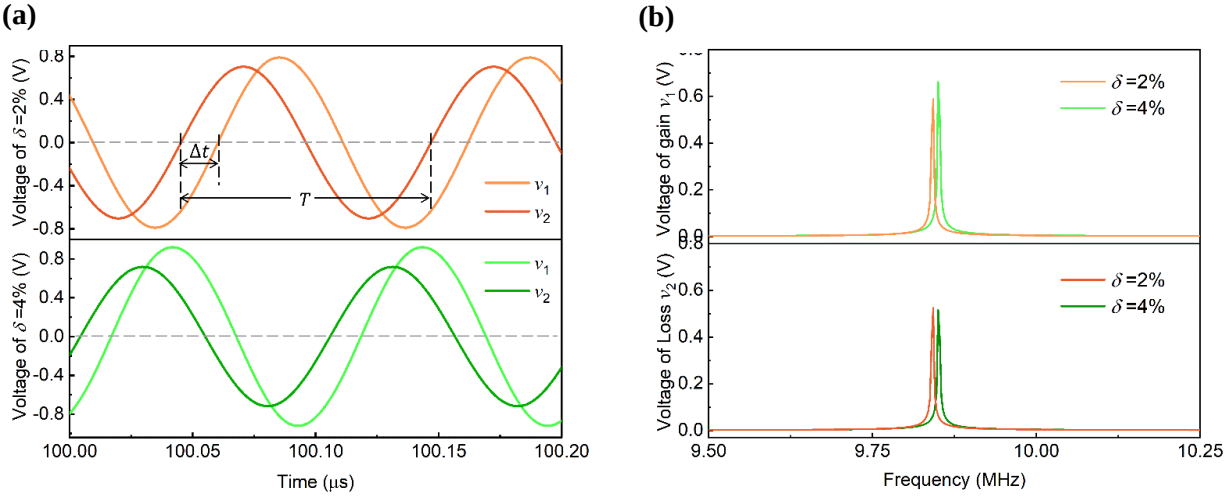

Supplementary Figure 13: Simulation results of PT-symmetric LC resonators using the ADS simulator ($\gamma = 0.08$ and $\mu \approx 0.09$). **(a)** Time-domain response of node voltage on the gain (v_1) and loss (v_2) side, when subjected to perturbations of 2% and 4% on the loss capacitance, respectively. Notably, the steady-state voltage on the loss side, v_2, precedes that of the gain side, v_1. The phase difference can be quantified by the ratio of the leading time, Δt, to the oscillation cycle, T. **(b)** The frequency spectrum response was derived through the Fourier transform of the time-domain waveform. After the perturbation, both the gain and loss resonators synchronized to the same frequency with steady-state oscillation

We have also simulated the time-domain response of our nonlinear PT-symmetric LC system in the absence of perturbation. Fig. S14a depicts the time-domain node voltage of the gain and loss resonators biased in the broken regimes ($\mu = 0.04$ and $\mu = 0.064$). A frequency spectrum analysis via fast Fourier transform (FFT) is provided in Fig. S14b. The nonlinear PT system oscillates at a steady state with a frequency $\lambda_b = 1 - \mu/2$ as a consequence of its gain saturation mechanism. The resonant frequency decreases with increasing the coupling coefficient.

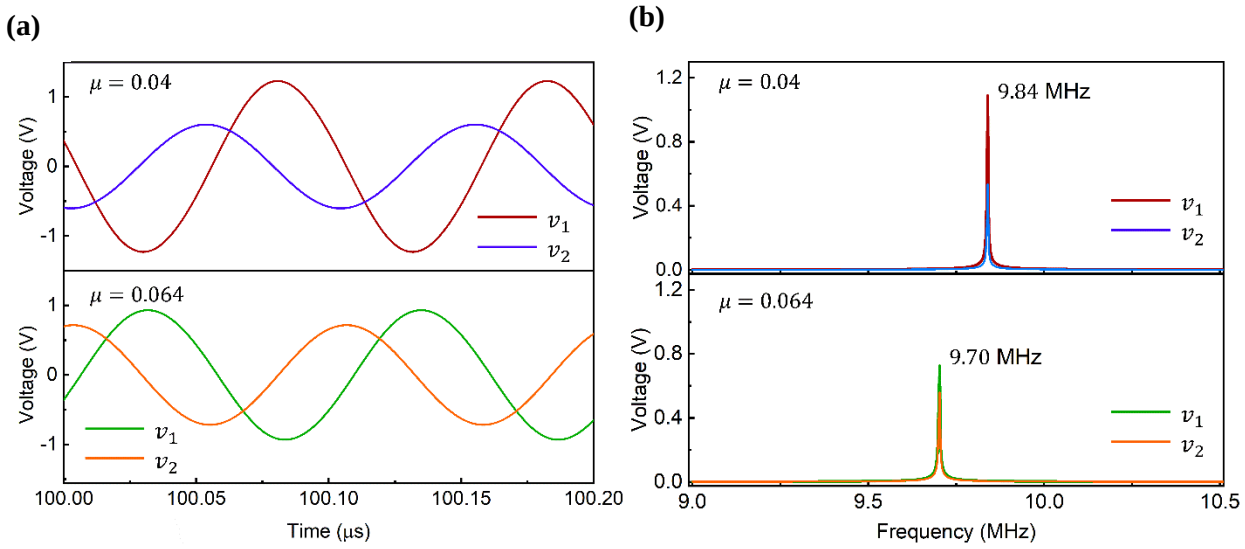

Supplementary Figure 14: Simulation results of nonlinear PT-symmetric LC resonators ($\gamma = 0.08, \mu = 0.04$ or $\mu = 0.064$). **(a)** Time-domain response of node voltage on the gain (v_1) and loss (v_2) side. **(b)** The frequency spectrum response was derived through the Fourier transform of the time-domain waveform.

(c) Transient simulations

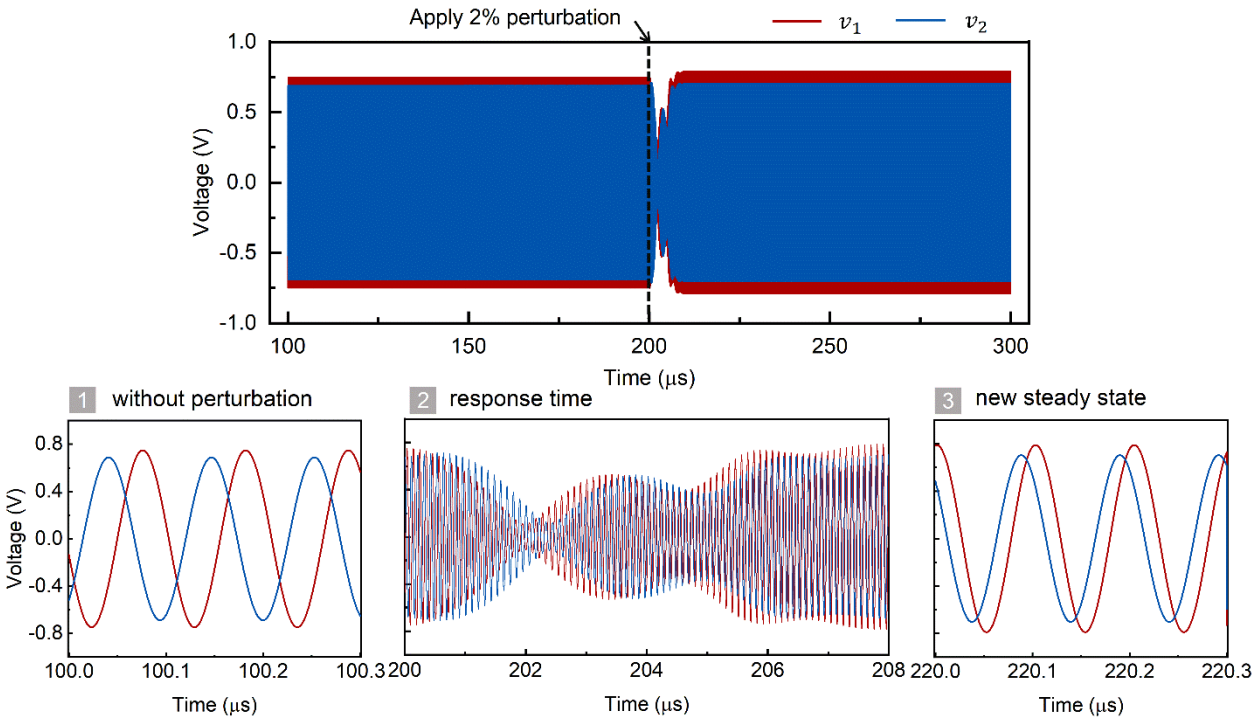

Supplementary Figure 15: The transient response characteristics are displayed when a 2% perturbation is applied to the loss resonator. The system undergoes an initial steady oscillation (stage 1), followed by an unsteady-state oscillation (stage 2), before establishing a new steady-state oscillation (stage 3). The red line indicates the voltage of the gain resonator, while the blue line represents the voltage of the loss side. The three insets provide magnified views of each stage within the entire time-domain waveform.

Fig. S15 depicts the time-domain voltage response when a perturbation is introduced to the system. In the simulation, a voltage-controlled switch was incorporated to regulate the 2% perturbation applied to the loss capacitance at t=200 μs. It can be observed that the perturbation disrupts the initial steady state. Subsequently, the system undergoes an unsteady-state oscillation with a response time of approximately 8 μs, and eventually evolves into a new steady state. The time-domain waveforms of stages 1 and 3 further demonstrate that the perturbation instigates changes in the phase difference between the gain (v_1) and loss (v_2) resonators.

S5. Experiment setup and measurements

(a) Experiment setup

We constructed a test platform, illustrated in Fig. S16, for our experiments. The parameters of the gain and loss resonators were set to $L_1 = L_2 = 1$ μH, $R_2 = 800$ Ω and $R_1 = -760$ Ω, respectively. The initial capacitance of the temperature sensor on the loss side was approximately 249 pF at 36℃. To achieve PT symmetry, we regulated an adjustable capacitor on the gain side. A DC source (Rigol DP832A) was employed to power the negative resistance circuit, while an oscilloscope (Keysight DSOX3024T) was used to record and analyze the time-domain voltage response of the gain and loss sides. Precise adjustment of the coupling capacitance was accomplished using an impedance analyzer (Hioki IM7580A) to evaluate the initial working condition. This allows the system to operate in the PT-symmetric regime near an EP, with the coupling coefficient $\gamma = R_2^{-1}\sqrt{L/C} \approx 0.08$, and the coupling coefficient μ was set to about 0.09. When a perturbation caused by a temperature change was applied to the loss side, the phase difference between the gain and loss resonator can be directly recorded via the oscilloscope.

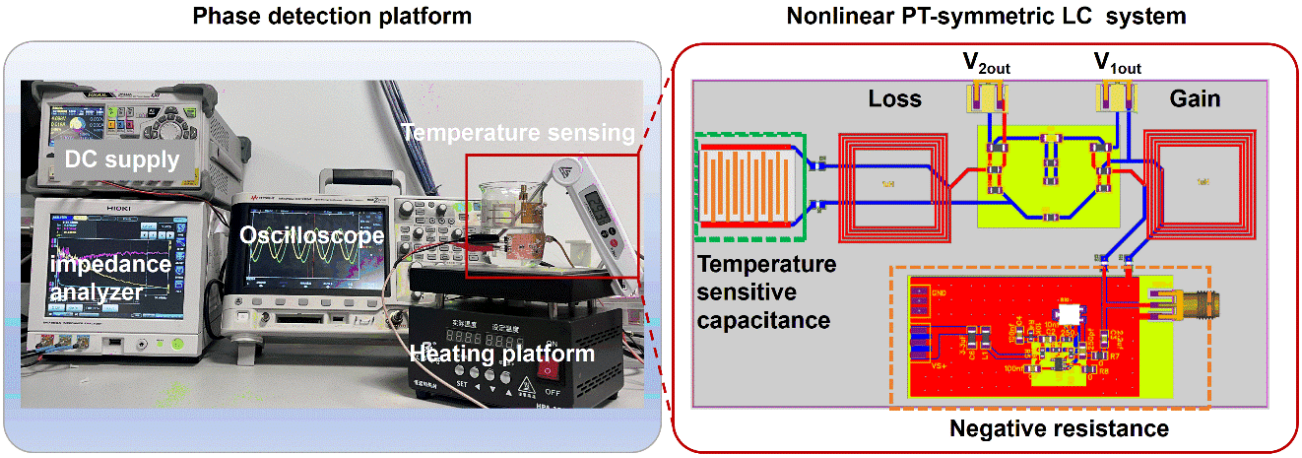

Supplementary Figure 16: Photograph of the experimental setup and instruments utilized for a PT symmetric LC system. These include a Direct Current (DC) power supply, an oscilloscope, a heating platform, an impedance analyzer, and a temperature sensor.

(b) A capacitance temperature sensor

Fig. S17a illustrates the structure of a temperature sensing capacitor. The interdigital structure was printed on the transparent, fully flexible printed circuit (FPC) surface and then coated with a polyethylene glycol (PEG 6000) sensitive material. During the experiment, the solid PEG was heated to 100 ℃ until it melted. Subsequently, the liquid PEG was dropped onto the interdigital capacitor plane and allowed to cool to room temperature in a windless environment. The entire temperature sensing capacitor was then encapsulated using a polyurethane (PU) membrane, an environmentally friendly material known for its excellent elasticity, moderate height, and high water resistance. The sensitive range of our temperature sensing capacitance is

determined by the dielectric constant sensitive range of PEG materials. For the experiment, we printed an interdigital capacitor with 20 pairs measuring 15 mm in length and 0.1 mm in width, and attached the complete temperature sensing capacitor to the outer wall of the beaker. As the water temperature in the beaker increased, the sensitive capacitance experienced changes, introducing positive perturbations of 0-3.95% into the system. Fig. S17b also presents the dimension parameters of the interdigital capacitor and square planar inductor.

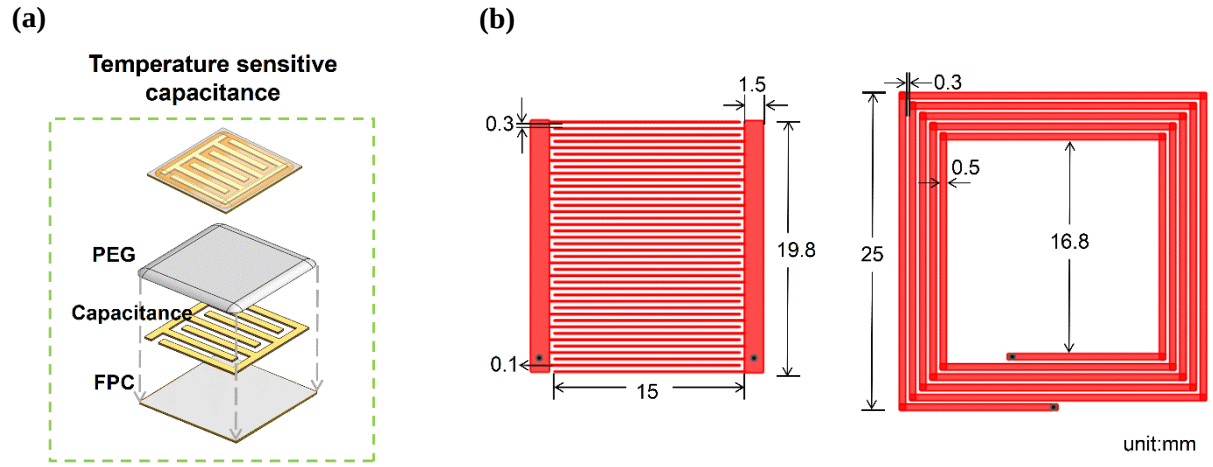

Supplementary Figure 17: (a) The schematic structure of a temperature sensing capacitor. It consists of polyethylene glycol (PEG) material, interdigital capacitance, and FPC. (b) The dimension parameters of the interdigital capacitor and square planar inductor.

(c) Measured phase difference as a function of temperature and the dynamic range

Fig. S18 shows the phase difference ϕ as a function of temperature T according to Fig. 2d in the main text. The dynamic range refers to the ratio between the maximum and the minimum perturbation that the sensor can sense, expressed as $Dr = 20\log\left(\frac{\delta_{max}}{\delta_{min}}\right)$. In our experiment, the dynamic perturbation range is estimated as $Dr = 20\log\left(\frac{0.0395}{8.3*10^{-5}}\right) = 53.5$ dB according to Fig. 2d in the main text.

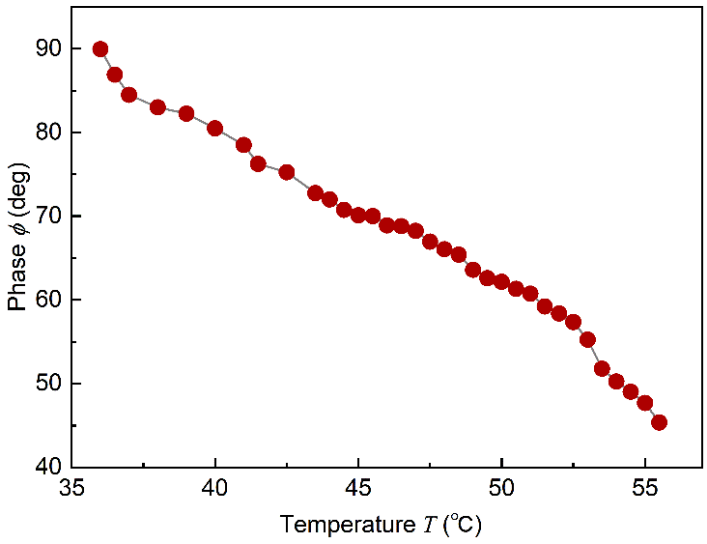

Supplementary Figure 18: The measured phase difference as a function of temperature.

References

1. Schindler, J. Lin, Z., Lee, J. M., Ramezani, H., Ellis, F. M. and Kottos, T. PT-symmetric electronics. *J. Phys.* **A45**, 444029 (2012).
2. Kononchuk, R., Cai, J., Ellis, F., Thevamaran, R. & Kottos, T. Exceptional-point-based accelerometers with enhanced signal-to-noise ratio. *Nature*, **607**, 697-702(2022).
3. Zhou, B. B., Wang, L.F., Dong, L. & Huang, Q. A. Observation of the perturbed eigenvalues of PT-symmetric *LC* resonator systems. *J. Phys. Commun.* **5**, 045010 (2021).
4. Assawaworrarit, S., Yu, X. & Fan, S. Robust wireless power transfer using a nonlinear parity–time-symmetric circuit. *Nature* **546**, 387–390 (2017).
5. Suntharalingam, A., Fernández-Alcázar, L., Kononchuk, R. & Kottos, T. Noise resilient exceptional-point voltmeters enabled by oscillation quenching phenomena. *Nat. Commun*. **14**, 5515 (2023).
6. Pipes, L.A. and Harvill, L.R. *Applied Mathematics for Engineers and Physicists*, pp.883-884 (McGraw-Hill, 1984).
7. Zhou, Y., Wang, H.Y., Wang, L. F., Dong, L. & Huang, Q.A. Experimental study of the nonlinear distortion of non-reciprocal transmission in nonlinear parity-time symmetric *LC* resonators. *Appl. Phys. Lett.* **122**, 233301 (2023).